

Central Lancashire Online Knowledge (CLoK)

Title	The bar rotation rate as a diagnostic of dark matter content in the centre of disc galaxies
Type	Article
URL	https://clock.uclan.ac.uk/id/eprint/45936/
DOI	https://doi.org/10.1093/mnras/stad646
Date	2023
Citation	Buttitta, C, Corsini, E M, Aguerri, J A L, Coccato, L, Costantin, L, Cuomo, V, Debattista, Victor P, Morelli, L and Pizzella, A (2023) The bar rotation rate as a diagnostic of dark matter content in the centre of disc galaxies. Monthly Notices of the Royal Astronomical Society. ISSN 0035-8711
Creators	Buttitta, C, Corsini, E M, Aguerri, J A L, Coccato, L, Costantin, L, Cuomo, V, Debattista, Victor P, Morelli, L and Pizzella, A

It is advisable to refer to the publisher's version if you intend to cite from the work.
<https://doi.org/10.1093/mnras/stad646>

For information about Research at UCLan please go to <http://www.uclan.ac.uk/research/>

All outputs in CLoK are protected by Intellectual Property Rights law, including Copyright law. Copyright, IPR and Moral Rights for the works on this site are retained by the individual authors and/or other copyright owners. Terms and conditions for use of this material are defined in the <http://clock.uclan.ac.uk/policies/>

The bar rotation rate as a diagnostic of dark matter content in the centre of disc galaxies

C. Buttitta¹,¹★ E. M. Corsini^{1,2},^{1,2}★ J. A. L. Aguerri³,³★ L. Coccato⁴,⁴ L. Costantin,⁵ V. Cuomo⁶,⁶ V. P. Debattista⁷,⁷ L. Morelli⁶ and A. Pizzella^{1,2}

¹Dipartimento di Fisica e Astronomia ‘G. Galilei’, Università di Padova, vicolo dell’Osservatorio 3, I-35122 Padova, Italy

²INAF – Osservatorio Astronomico di Padova, vicolo dell’Osservatorio 2, I-35122 Padova, Italy

³Instituto de Astrofísica de Canarias, Calle Vía Láctea s/n, E-38205 La Laguna, Tenerife, Spain

⁴European Southern Observatory, Karl-Schwarzschild-Strasse 2, D-85748 Garching, Germany

⁵Centro de Astrobiología (CSIC-INTA), Ctra de Ajalvir km 4, Torrejón de Ardoz, E-28850 Madrid, Spain

⁶Instituto de Astronomía y Ciencias Planetarias, Universidad de Atacama, Avenida Copayapu 485, Copiapó, Chile

⁷Jeremiah Horrocks Institute, University of Central Lancashire, PR1 2HE Preston, UK

Accepted 2023 February 23. Received 2023 February 5; in original form 2022 December 20

ABSTRACT

We investigate the link between the bar rotation rate and dark matter content in barred galaxies by concentrating on the cases of the lenticular galaxies NGC 4264 and NGC 4277. These two gas-poor galaxies have similar morphologies, sizes, and luminosities. But, NGC 4264 hosts a fast bar, which extends to nearly the corotation, while the bar embedded in NGC 4277 is slow and falls short of corotation. We derive the fraction of dark matter $f_{\text{DM, bar}}$ within the bar region from Jeans axisymmetric dynamical models by matching the stellar kinematics obtained with the MUSE integral-field spectrograph and using SDSS images to recover the stellar mass distribution. We build mass-follows-light models as well as mass models with a spherical halo of dark matter, which is not tied to the stars. We find that the inner regions of NGC 4277 host a larger fraction of dark matter ($f_{\text{DM, bar}} = 0.53 \pm 0.02$) with respect to NGC 4264 ($f_{\text{DM, bar}} = 0.33 \pm 0.04$) in agreement with the predictions of theoretical works and the findings of numerical simulations, which have found that fast bars live in baryon-dominated discs, whereas slow bars experienced a strong drag from the dynamical friction due to a dense DM halo. This is the first time that the bar rotation rate is coupled to $f_{\text{DM, bar}}$ derived from dynamical modelling.

Key words: galaxies: bar – galaxies: formation – galaxies: individual: NGC 4264 – galaxies: individual: NGC 4277 – galaxies: kinematics and dynamics – galaxies: structure.

1 INTRODUCTION

About two-thirds of disc galaxies, including the Milky Way, have a bar which is tumbling at the centre of the disc (Aguerre, Méndez-Abreu & Corsini 2009; Buta et al. 2015). The bar is an efficient agent for redistributing the stars by exchanging angular momentum, energy, and mass among the different galactic components including the dark matter (DM) halo (Athanasoula, Machado & Rodionov 2013; Sellwood 2014).

The main properties of bars are the radius R_{bar} , which defines the elongation of the stellar orbits in the bar, strength S_{bar} , which quantifies the non-axisymmetric contribution of the bar to the gravitational potential, pattern speed Ω_{bar} , which is the angular frequency of the bar figure rotation, and the rotation rate \mathcal{R} . The latter is defined as the dimension-less ratio between the length of the corotation radius R_{cor} , where stars circle the galactic centre at Ω_{bar} , and bar radius. The rotation rate does not depend on galaxy distance and distinguishes between fast ($1 \leq \mathcal{R} \leq 1.4$) and slow bars ($\mathcal{R} > 1.4$) (Athanasoula 1992; Debattista & Sellwood 2000).

The two main mechanisms which trigger the formation of a bar are internal gravitational instabilities of the stellar disc (Sellwood 1981) and external tidal interactions (Noguchi 1987). Spontaneously formed bars are usually thin, long, and fast (Athanasoula et al. 2013), whereas tidally induced bars are thick, short, and slow (Martinez-Valpuesta et al. 2017). The bar properties evolve with time reshaping the morphology, orbital structure, mass distribution, star formation, and stellar population properties of their host galaxies (Laurikainen et al. 2007; Fragkoudi, Athanasoula & Bosma 2016). Once formed, the bar becomes longer and stronger and it slows down on time-scales, which depend on the DM content in the disc region (Debattista & Sellwood 1998, 2000; Athanasoula & Misiriotis 2002; Petersen, Weinberg & Katz 2019).

In the last decade, the systematic investigation of the pattern speeds of large samples of barred galaxies with integral-field spectroscopy has shown that almost all bars are fast (Aguerre et al. 2015; Guo et al. 2019; Cuomo et al. 2020; Garma-Oehmichen et al. 2020, 2022) confirming the early findings based on long-slit spectroscopy of few selected objects (Corsini 2011). This supports the idea that the central regions of lenticular and spiral galaxies host maximal (or nearly maximal) stellar discs with a low content of DM.

These observationally driven findings are in conflict with the predictions of some hydrodynamical cosmological simulations, for

* E-mail: chiara.buttitta@gmail.com (CB); enricomaria.corsini@unipd.it (EMC); jalfonso@iac.es (JALA)

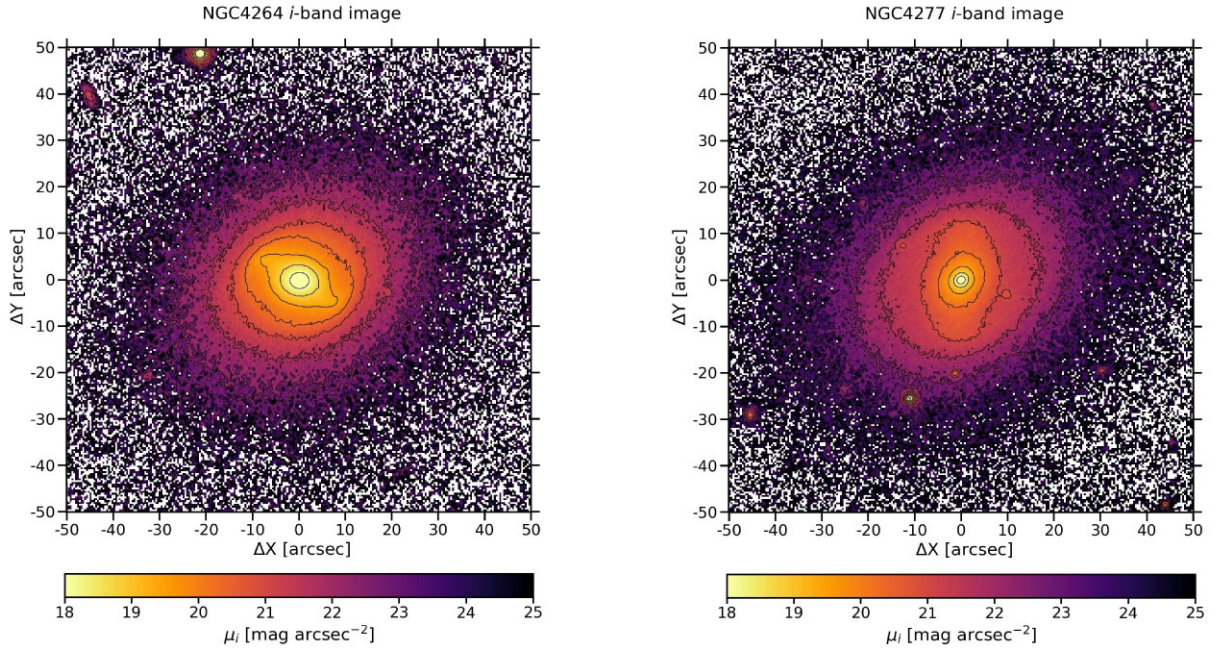


Figure 1. SDSS *i*-band image of NGC 4264 (left-hand panel) and NGC 4277 (right-hand panel). Some reference isophotes, spaced by $0.5 \text{ mag arcsec}^{-2}$, are overlaid with black lines. The FOV is $1.7 \times 1.7 \text{ arcmin}^2$ and is oriented with North up and East left.

which galaxies are embedded in centrally concentrated DM haloes required by the Λ CDM paradigm. Algorry et al. (2017) measured the bar properties in the galaxies extracted from the EAGLE simulation (Schaye et al. 2015) and found a reasonable agreement with the bar radii and strengths measured for real galaxies. However, the simulated bars experienced an intense slowdown due to the dynamical friction of the DM halo and many of them ended up slow at $z \sim 0$. Similarly, Roshan et al. (2021) found that the bars in the TNG50 simulation (Nelson et al. 2018; Pillepich et al. 2018) are much slower ($\mathcal{R} > 1.9$) with respect to the observed ones. More recently, the discrepancy between observations and simulations has been attenuated by the findings of Fragkoudi et al. (2021) and Marioni et al. (2022). Fragkoudi et al. (2021) analysed the barred galaxies in the AURIGA simulation suite (Grand et al. 2017) and showed that they have fast bars because they are more baryon-dominated with respect to those in the TNG simulation. Marioni et al. (2022) investigated the evolution of barred galaxies in the CLUES simulation (Gottloeber, Hoffman & Yepes 2010), which have shorter, but not slower, bars with respect to their observed counterparts. A possible explanation for these findings could reside in the different ingredients of the simulations so far analysed, including the resolution of the simulation and the gas fraction, disc thickness, stellar and AGN feedback, and baryonic content of the simulated galaxies.

Dynamical models of barred galaxies with accurate measurements of Ω_{bar} and \mathcal{R} are needed to rigorously test the predictions of numerical simulations regarding the bar properties as a function of gas content, luminosity, and DM distribution. In this paper, we derive the mass distribution of two barred galaxies, NGC 4264 and NGC 4277, for which the values of Ω_{bar} are amongst the best-constrained ones ever obtained with direct measurements (Tremaine & Weinberg 1984). This will allow us to investigate the link between \mathcal{R} and the DM content in the bar region because NGC 4264 hosts a fast bar ($\mathcal{R} = 0.9 \pm 0.2$; Cuomo et al. 2019a) while the bar in NGC 4277 is slow ($\mathcal{R} = 1.8_{-0.3}^{+0.5}$; Buttitta et al. 2022). We aim at understanding whether a larger value of \mathcal{R} results from the effective bar braking

due to the dynamical friction exerted by the DM halo and therefore is a diagnostic of a large content of DM in the bar region.

The paper is organized as follows. We present the main properties of the two galaxies and their bars in Sections 2 and 3, respectively. We discuss the choice and application of the dynamical model in Section 4. We present our results and their implications in Sections 5 and 6, respectively.

2 MAIN PROPERTIES OF NGC 4264 AND NGC 4277

NGC 4264 and NGC 4277 are two early-type disc galaxies classified as SB0⁺(rs) and SAB(rs)0/a, respectively, by de Vaucouleurs et al. (1991, hereafter RC3). They have a quite similar morphology (Fig. 1) with a well-defined bar surrounded by a pseudo-ring and oriented at an intermediate position angle with respect to the major and minor axes of the disc ($|\text{PA}_{\text{bar}} - \text{PA}_{\text{disc}}| \sim 50^\circ$). The bar region appears to be mostly free of dust and star formation and the disc has an intermediate inclination ($i_{\text{disc}} \sim 40^\circ$). NGC 4264 and NGC 4277 have similar luminosity and size, as calculated from the apparent corrected magnitude B_{T}^0 (RC3) and galaxy diameters D_{25} and d_{25} (RC3) by adopting the distance obtained from the radial velocity with respect to the cosmic microwave background reference frame (Fixsen et al. 1996). NGC 4264 and NGC 4277 are located behind the Virgo cluster. They likely form an interacting couple with the giant elliptical galaxy NGC 4261 (Schmitt 2001) and with the spiral galaxy NGC 4273 (Kim et al. 2014), respectively. The main properties of both galaxies are given in Table 1.

3 PROPERTIES OF THE BARS

Cuomo et al. (2019a) and Buttitta et al. (2022) analysed the surface photometry and integral-field spectroscopy of NGC 4264 and NGC 4277, respectively, to characterize the properties of their bars. They measured the bar radius and strength from the surface

Table 1. Galaxy and bar properties of NGC 4264 and NGC 4277. (1): Morphological type from RC3. (2): Total absolute magnitude from B_T^0 in RC3. (3): Distance calculated from the radial velocity with respect to the cosmic microwave background reference frame (Fixsen et al. 1996) and assuming $H_0 = 75 \text{ km s}^{-1} \text{ Mpc}^{-1}$, $\Omega_m = 0.308$, and $\Omega_\Lambda = 0.692$. (4): Major and minor diameters of the isophote with surface brightness $\mu_B = 25 \text{ mag arcsec}^{-2}$ from RC3. (5): Disc position angle from the isophotal analysis. (6): Disc inclination from the isophotal analysis assuming an infinitesimally thin disc. (7): Bar position angle from the photometric decomposition. (8): Bar radius. (9): Bar strength. (10): Circular velocity from the stellar streaming motion corrected for asymmetric drift. (11): Bar pattern speed. (12): Corotation radius. (13): Bar rotation rate.

Property		NGC 4264	NGC 4277
(1)	Morph. Type	SB0 ⁺ (rs)	SAB(rs)0/a
(2)	M_{BT}^0 (mag)	−19.20	−19.27
(3)	D (Mpc)	38.0 ± 2.7	33.8 ± 2.4
(4)	$D_{25} \times d_{25}$ (kpc ²)	10.8×8.8	10.3×8.6
(5)	PA_{disc} (°)	114.0 ± 1.2	123.3 ± 0.3
(6)	i_{disc} (°)	36.7 ± 0.7	40.7 ± 0.7
(7)	PA_{bar} (°)	56.4 ± 0.1	175.59 ± 0.04
(8)	R_{bar} (kpc)	3.2 ± 0.5	$3.2_{-0.6}^{+0.9}$
(9)	S_{bar} –	0.31 ± 0.04	0.21 ± 0.02
(10)	V_{circ} (km s ^{−1})	189 ± 10	148 ± 5
(11)	Ω_{bar} (km s ^{−1} kpc ^{−1})	71 ± 4	25 ± 3
(12)	R_{cor} (kpc)	2.8 ± 0.2	6.0 ± 0.9
(13)	\mathcal{R} –	0.9 ± 0.2	$1.8_{-0.3}^{+0.5}$

photometry obtained from broad-band imaging of the Sloan Digital Sky Survey (SDSS). They derived the bar pattern speed from the stellar kinematics obtained from integral-field spectroscopy performed with the Multi-Unit Spectroscopic Explorer (MUSE) at the Very Large Telescope (VLT). They also estimated the corotation radius from the circular velocity, which they constrained by correcting the stellar streaming motions for asymmetric drift. Finally, they derived the bar rotation rate. Here, we provide a concise description of the acquisition and analysis of the photometric and kinematic data and a summary of the results. The properties of the bars of both galaxies are given in Table 1.

3.1 Bar radius and strength

Cuomo et al. (2019a) and Buttitta et al. (2022) analysed the flux-calibrated *i*-band images of both galaxies available in the science archive of the SDSS Data Release 14 (Abolfathi et al. 2018). They were obtained with a spatial sampling of $0.3961 \text{ arcsec pixel}^{-1}$, total exposure time of 53.9 s, and seeing FWHM $\sim 1.5 \text{ arcsec}$. The images were sky subtracted and trimmed selecting a field of view (FOV) of $800 \times 800 \text{ pixel}^2$ centred on the galaxies corresponding to $5.3 \times 5.3 \text{ arcmin}^2$.

The isophotal analysis recovered the geometric parameters PA_{disc} and i_{disc} of the galaxy disc, which were adopted to deproject the galaxy image. The photometric decomposition was performed to estimate the position angle, PA_{bar} , of the bar and its contribution to the galaxy surface brightness.

For both galaxies, the radius R_{bar} of the bar was derived as the mean of the estimates obtained from the analysis of the radial profile of the position angle of the interpolated isophotes on the deprojected image as in Aguerri, Debattista & Corsini (2003), of the intensity contrast between the bar and interbar regions following Aguerri, Muñoz-Tuñón & Varela (2000), and of the photometric

decomposition adopting a Ferrers bar as in Méndez-Abreu et al. (2017). The strength S_{bar} of the bar was derived as the mean of the values obtained from the Fourier analysis of the deprojected image as in Athanassoula & Misiriotis (2002) and from the bar axial ratio as in Aguerri et al. (2009). The $\pm\sigma$ errors on R_{bar} and S_{bar} were estimated by calculating the difference between the adopted value and the highest/lowest measure. The two bars have lengths consistent with the median value found for SB0 galaxies (Aguerre et al. 2009) and are both weak according to the classification of Cuomo et al. (2019b).

3.2 Bar pattern speed and rotation rate

The integral-field spectroscopy was carried out with the wide field mode of MUSE (Prog. Id. 094.B-0241(A); P.I.: E.M. Corsini) mapping a nominal FOV of $1 \times 1 \text{ arcmin}^2$ with a spatial sampling of $0.2 \text{ arcsec pixel}^{-1}$ and covering the wavelength range of 4800–9300 Å with a spectral sampling of $1.25 \text{ Å pixel}^{-1}$ and a nominal spectral resolution of FWHM = 2.51 Å. The mean value of the seeing during the observations was FWHM $\sim 1.1 \text{ arcsec}$. The observations were split into different observing blocks which were mosaiced to fully map the galaxies along their photometric major axis for an actual FOV coverage of $1.0 \times 1.7 \text{ arcmin}^2$.

Cuomo et al. (2019a) and Buttitta et al. (2022) measured the stellar and ionized-gas kinematics of the two galaxies by using the PPIX (Cappellari & Emsellem 2004) and GANDALF (Sarzi et al. 2006) codes. The spaxels in the datacube were spatially binned with the Voronoi tessellation algorithm (Cappellari & Copin 2003) to ensure a target signal-to-noise ratio $S/N = 40$ per bin. In each bin, the galaxy spectrum was fitted by convolving the spectra extracted from the ELODIE stellar library ($\sigma_{\text{instr}} = 13 \text{ km s}^{-1}$; Prugniel & Soubiran 2001) with a line-of-sight velocity distribution (LOSVD) modelled with a truncated Gauss–Hermite series (Gerhard 1993; van der Marel & Franx 1993) in the wavelength range 4800–5600 Å. The circular velocity V_{circ} was derived by correcting the stellar streaming motion for the asymmetric drift (Binney & Tremaine 1987).

The pattern speed Ω_{bar} of both bars was obtained by applying the Tremaine–Weinberg method (Tremaine & Weinberg 1984) on the reconstructed image and stellar velocity field of the host galaxies. The value of Ω_{bar} is given by $\langle V \rangle = \langle X \rangle \sin(i_{\text{disc}}) \Omega_{\text{bar}}$. It depends on the disc inclination and on the luminosity-weighted position $\langle X \rangle$ and LOS velocity $\langle V \rangle$ of the stellar component within apertures parallel to the disc major axis and crossing the bar. Finally, the corotation radius R_{cor} and the rotation rate \mathcal{R} values were estimated calculating $R_{\text{cor}} = V_{\text{circ}}/\Omega_{\text{bar}}$ and $\mathcal{R} = R_{\text{cor}}/a_{\text{bar}}$, respectively. The errors on R_{cor} and \mathcal{R} were estimated by using Monte Carlo simulations. We generated a distribution of R_{cor} and \mathcal{R} by accounting for the errors on R_{bar} , i_{disc} , and V_{circ} . The adopted $\pm\sigma$ errors for R_{cor} and \mathcal{R} are calculated as the 16th and 84th percentiles of the distributions.

The two galaxies have similar properties in terms of bar size and strength, but not in terms of bar pattern speed: NGC 4264 hosts a fast bar ($\mathcal{R} = 0.9 \pm 0.2$) while the bar in NGC 4277 is slow ($\mathcal{R} = 1.8_{-0.3}^{+0.5}$). The different bar rotation rates could be due to a different bar formation mechanism and/or a different DM content in the bar region.

Although NGC 4264 possibly forms an interacting pair with NGC 4261, which is located at a projected distance of 3.5 arcmin (Schmitt 2001), which corresponds to a quite large physical distance of 4.9 Mpc, it lacks a strongly disturbed morphology. According to Cuomo et al. (2019a), this suggests that the interaction is weak and not responsible for having triggered the bar formation in NGC 4264. NGC 4277 is likely paired with NGC 4273, which is located at a

projected distance of 1.9 arcmin (van Driel et al. 2000) corresponding to a physical distance of 2.5 Mpc. Buttitta et al. (2022) argued that the bar formation in NGC 4277 could have been triggered by their tidal interaction or alternatively, the bar could have been braked by the dynamical friction of a dense DM halo (Debattista et al. 2006; Athanassoula et al. 2013).

4 STELLAR DYNAMICAL MODEL

4.1 Jeans dynamical models

Reconstructing the mass distribution of a disc galaxy using unresolved stars as tracers of the gravitational potential is a challenging task due to the non-uniqueness of the light deprojection (Rybicki 1987; Gerhard & Binney 1996). The bar introduces a further complication since its characterization requires two additional parameters: the orientation and figure rotation (Lablanche et al. 2012). This increases the degeneracy between the model parameters with different combinations able to reproduce the observed photometric and kinematic properties of the galaxy.

Several methods have been developed to recover the dynamical structure of a galaxy from broad-band imaging and long-slit/integral-field spectroscopy, but the dynamical modelling of barred galaxies is still at an early stage. The recently developed orbit-superposition Schwarzschild models by Vasiliev & Valluri (2020) and Tahmasebzadeh et al. (2022), which to date have been applied only to data from N -body simulations, considered the bar pattern speed. Portail et al. (2016) built a dynamical model of the Milky Way to recover its bar pattern speed by using the made-to-measure method as implemented by de Lorenzi et al. (2007).

In general, barred galaxies have been modelled with axisymmetric dynamical models, including the Jeans Anisotropic Modelling (JAM; Cappellari 2008, 2020), which has been extensively applied to spectroscopic surveys of nearby lenticular and spiral galaxies (e.g. Williams, Bureau & Cappellari 2009; Cappellari et al. 2013; Guo et al. 2019). It models the LOS second velocity moment for galaxies with an axisymmetric mass distribution, including a DM halo, to be compared with the root-mean-square velocity V_{rms} derived from the observed velocity V_{los} and velocity dispersion σ_{los} . JAM requires the surface-brightness distribution of the galaxy to be described through a Multi-Gaussian Expansion (MGE; Cappellari 2002) parametrization, which simplifies the solution of Jeans equations to recover the galaxy inclination i , mass-to-light ratio $(M/L)_*$ of the matter following the light (which may include DM as well as stars), and anisotropy parameter $\beta_z = 1 - \sigma_z^2/\sigma_R^2$, where σ_R and σ_z are the radial and vertical components of the velocity dispersion, respectively, in a cylindrical coordinate system with the origin in the centre of the galaxy and symmetry axis aligned with its rotation axis.

Cappellari (2008) compared the JAM and orbit-superposition Schwarzschild models of six fast-rotating lenticular galaxies from the SAURON survey (de Zeeuw et al. 2002). They have *HST* and ground-based photometry and SAURON integral-field spectroscopy. The values of β_z from JAM are consistent within the uncertainties with those obtained with the Schwarzschild modelling. Since fast rotators show a slightly positive value of β_z , the inclination-anisotropy degeneracy was removed, constraining $\beta_z > 0$. Although there is a small dependence on the anisotropy parameter, overall the $(M/L)_*$ values and mass models obtained with the two approaches are also in agreement. This means that the JAM model, with simple and well-motivated assumptions, provides a reasonable description of the mass distribution of lenticular galaxies.

Cappellari et al. (2013) applied the JAM algorithm to 260 nearby early-type galaxies of the ATLAS^{3D} survey (Cappellari et al. 2011), whose surface-brightness distribution was measured from SDSS and Isaac Newton Telescope imaging and the stellar kinematics were traced out to roughly one effective radius R_e with SAURON integral-field spectroscopy. This volume-limited sample was composed of galaxies with a distance $D < 42$ Mpc, absolute magnitude $M_K < -21.5$ mag, and stellar mass $M_* \gtrsim 6 \times 10^9 M_\odot$. The stellar kinematics of most of the sample galaxies are reasonably well reproduced by mass-follows-light models, suggesting that early-type galaxies have a simple internal structure within $1R_e$, and that the DM halo is not dominant. By adding the contribution of a NFW (Navarro, Frenk & White 1995) DM halo, Cappellari et al. (2013) estimated a median DM fraction within the effective radius of $f_{\text{DM}}(r < R_e) = 0.13$. About one-third of the sample galaxies host a bar and for some of them, the quality of the fit was poor due to the low S/N and/or twisted stellar kinematics or the presence of a strong bar. The recovered values of $(M/L)_*$ for the whole sample have an accuracy of 6 per cent, which falls to 15 per cent for the barred galaxies.

Lablanche et al. (2012) analysed realistic simulations of two SB0 galaxies to explore the reliability of the JAM approach in recovering the dynamical parameters of a barred galaxy. The simulated galaxies mimicked NGC 4442 and NGC 4754 and were projected at different disc inclinations ($i_{\text{disc}} = 25^\circ, 45^\circ, 60^\circ$, and 87°) and with different bar orientation ($|\text{PA}_{\text{bar}} - \text{PA}_{\text{disc}}| = 18^\circ, 45^\circ, 60^\circ$, and 87°). In general, i_{disc} can be recovered with JAM although this result is biased by the non-uniqueness of the mass deprojection in nearly face-on or edge-on barred systems (with a maximum error $\Delta i_{\text{disc}} \sim 6^\circ$ for edge-on systems). The value of β_z is not well recovered for any disc inclination and bar orientation, because the bar produces a deprojected mass density which is flatter or rounder with respect to the azimuthally averaged one when the bar is viewed side-on or end-on, respectively. This issue is not unique to JAM, but is expected to affect also the axisymmetric dynamical models based on orbit superposition. The recovered M/L depends on the disc inclination and bar orientation. The uncertainty is smaller than 1.5 per cent for systems with $i_{\text{disc}} \geq 45^\circ$ and $|\text{PA}_{\text{bar}} - \text{PA}_{\text{disc}}| = 60^\circ$ and it never exceeds 3 per cent for the other inclinations. The recovered $(M/L)_*$ is underestimated (overestimated) if $\text{PA}_{\text{disc}} < 45^\circ$ ($\text{PA}_{\text{disc}} > 45^\circ$). In their tests, they found that the maximum systematic error of 15 per cent on $(M/L)_*$ occurs when the bar is seen nearly end-on ($\text{PA}_{\text{bar}} = 18^\circ$) or side-on ($\text{PA}_{\text{bar}} = 87^\circ$). They also investigated how the size of the FOV affects the recovered parameters, and concluded that if the FOV extends out to the bar radius, the systematic uncertainty on $(M/L)_*$ decreases and tends to a limiting value of 10 per cent. However, the mass models of Lablanche et al. (2012) did not include DM haloes.

We adopted the JAM method to recover the mass distribution of NGC 4264 and NGC 4277, since we are confident that applying such an axisymmetric dynamical model gives a reliable estimate of $(M/L)_*$ and DM fraction even in barred galaxies. Both objects are ideal targets according to Lablanche et al. (2012), because they have an intermediate inclination ($i_{\text{disc}} \sim 40^\circ$), are not substantially affected by dust, and host a weak bar with an intermediate orientation with respect to the disc major and minor axis ($|\text{PA}_{\text{bar}} - \text{PA}_{\text{disc}}| \sim 50^\circ$). According to Lablanche et al. (2012), in this configuration, we expect to systematically overestimate the $(M/L)_*$ by a factor of 10 per cent. This translates into a larger overestimate of the DM fraction in galaxies with a larger content of luminous matter. In addition, the fine spatial sampling, wide FOV, and high spectral resolution of the MUSE integral-field spectrograph made it possible to accurately map the stellar kinematics throughout the galaxy disc. The kinematic maps do not show strong perturbed features as prescribed to minimize

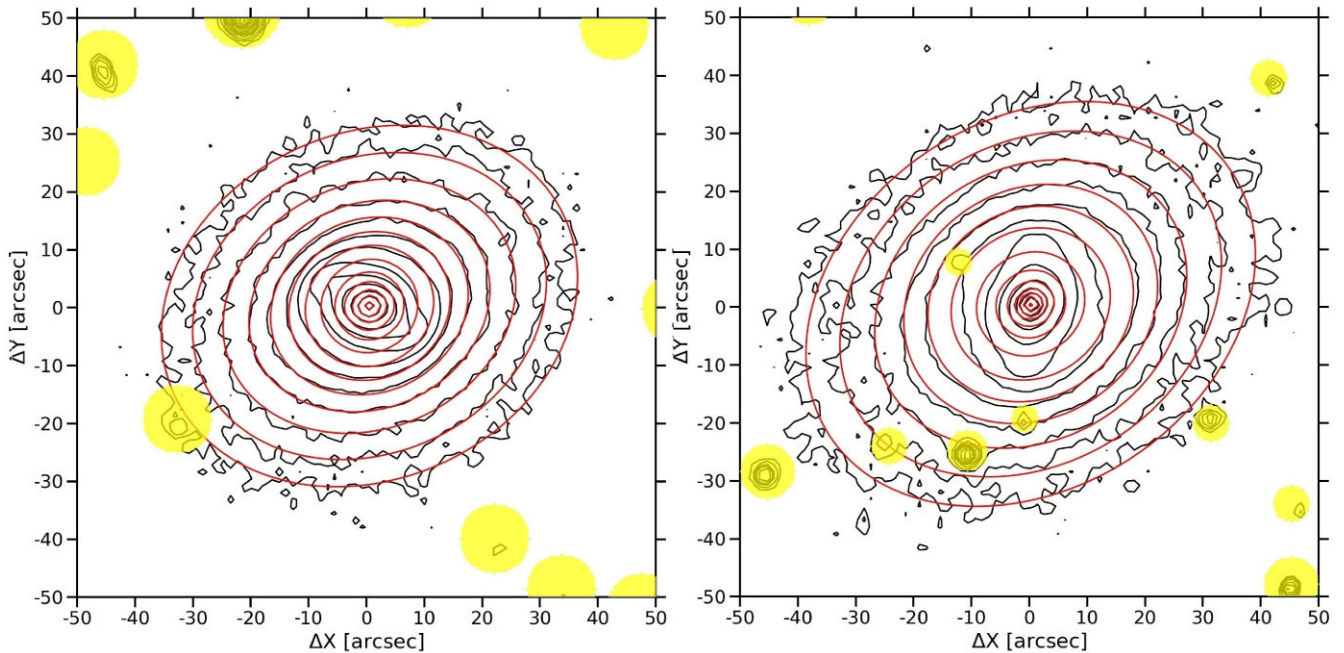


Figure 2. Some reference isophotes for the SDSS *i*-band image (black lines) and MGE model (red lines) of NGC 4264 (left-hand panel) and NGC 4277 (right-hand panel). The FOV is 1.7×1.7 arcmin² and oriented with North up and East left. Flux levels are normalized to the central surface brightness of the image and the contours are spaced by $0.5 \text{ mag arcsec}^{-2}$. While the MGE model was constrained using the original image, the image shown here is binned by $3 \times 3 \text{ pixels}^2$ to reduce the noise for comparison purposes only. The yellow circles correspond to masked regions.

the biases in the estimation of the dynamical parameters. Finally, we notice that NGC 4264 and NGC 4277 have similar luminosities to those of NGC 4442 and NGC 4754. This gives us confidence in extending the findings of Lablanche et al. (2012) to our galaxies.

4.2 Multi-Gaussian expansion

To obtain a model for the luminosity volume density of both NGC 4264 and NGC 4277, we started by parametrizing the *i*-band surface brightness of the sky-subtracted SDSS image of each galaxy as the sum of a set of Gaussian components by using the MGE Python code, which is based on Cappellari (2002). The MGE method allows for a simple reconstruction of the intrinsic surface brightness distribution provided that the point spread function (PSF) can be approximated as a sum of Gaussian components. The intrinsic surface brightness distribution is then easily deprojected into the luminosity volume density, which is also parametrized as the sum of a set of Gaussian components.

We adopted the centre coordinates derived for the two galaxies by Cuomo et al. (2019a) and Buttitia et al. (2022). We estimated the root mean square of the sky surface brightness by performing a statistical analysis on different regions of the images containing exclusively the sky contribution. These areas were selected in empty regions, which were free of objects and far from the target galaxy to avoid the contamination of the light of field stars and background galaxies, as well as of the galaxy itself. Finally, we modelled the PSF by applying the MGE algorithm on a bright, isolated, and round-shaped field star constraining the best-fitting Gaussians to have a perfect circular shape. The surface brightness distribution of NGC 4264 is characterized by an isophotal twist in the outermost regions. The internal ($\text{PA}_{\text{in}} = 114^\circ 0 \pm 1^\circ 2$) and external regions ($\text{PA}_{\text{out}} = 122^\circ 8 \pm 2^\circ 4$) of the disc have different orientations but the same shape ($\epsilon = 0.20 \pm 0.02$) as found by Cuomo et al. (2019a). They argued that the isophotal outer twist is not representative of the actual

orientation of the disc. We decided to constrain the Gaussians with the geometric parameters of the internal disc which is mapped by the measured stellar kinematics. The radial profiles of PA and ϵ derived by Buttitia et al. (2022) from the surface brightness distribution of NGC 4277 show a clear disc-dominated region with a well-defined orientation ($\text{PA} = 123^\circ 3 \pm 0^\circ 3$) and shape ($\epsilon = 0.24 \pm 0.02$).

We obtained the MGE best-fitting model to the galaxy surface brightness by keeping constant the centre and position angle of the Gaussians derived by Cuomo et al. (2019a) and Buttitia et al. (2022), while further restricting the range of the resulting axial ratios of the Gaussian components to $[q_{\text{min}}, 1]$, where $q_{\text{min}} = 1 - \epsilon_{\text{disc}}$. This ensured that the permitted galaxy inclinations were not limited to a narrower range than that allowed by the data (e.g. Scott et al. 2013; Pagotto et al. 2019).

We show a few representative isophotes of the *i*-band images of NGC 4264 and NGC 4277 and compare these to the corresponding MGE best-fitting contours in Fig. 2. The MGE algorithm provided the total luminosity in counts, root mean square in pixels, and axial ratio for each best-fitting Gaussian parametrizing the intrinsic surface brightness distribution. We converted the output parameters into physical units by using the flux calibration and spatial scale of the images given by Cuomo et al. (2019a) and Buttitia et al. (2022) and correcting for cosmological dimming, *K*-correction (Chilingarian & Zolotukhin 2012), and Galactic extinction (Schlafly & Finkbeiner 2011). We adopted $M_{i,\odot} = 4.53 \text{ mag}$ as the absolute magnitude of the Sun in the SDSS *i*-band (Willmer 2018). We list the MGE best-fitting parameters of the intrinsic surface brightness distribution of NGC 4264 and NGC 4277 in Table 2.

4.3 Axisymmetric Jeans anisotropic model

With the MGE models at hand, we proceeded to use the JAM Python code based on Cappellari (2008) to build Jeans axisymmetric

Table 2. Best-fitting parameters of the Gaussian components in the MGE model of the *i*-band surface brightness distribution of NGC 4264 and NGC 4277. (1): Central luminosity surface density. (2) Standard deviation. (3) Axial ratio.

NGC 4264			NGC 4277		
I_0 ($L_\odot \text{ pc}^{-2}$)	σ (kpc)	q	I_0 ($L_\odot \text{ pc}^{-2}$)	σ (kpc)	q
(1)	(2)	(3)	(1)	(2)	(3)
15427.0	0.04	0.80	5106.5	0.08	0.88
4309.5	0.13	0.80	1023.8	0.20	0.85
691.4	0.34	0.80	353.5	0.48	0.92
1141.1	0.43	1.00	158.6	1.52	0.91
443.8	1.01	1.00	41.9	3.78	0.76
219.3	1.72	0.80	–	–	–
64.8	3.86	0.81	–	–	–

dynamical models for NGC 4264 and NGC 4277 in order to derive the DM content within the bar region.

We selected the best-fitting JAM model by minimizing the χ^2 difference between the predicted second moment of the velocity field and MUSE stellar kinematics measured by Cuomo et al. (2019a) and Buttitta et al. (2022). To this aim, we obtained, for each spatial bin, the observed V_{rms} as

$$V_{\text{rms}} \equiv \sqrt{V_{\text{los}}^2 + \sigma_{\text{los}}^2}$$

and its corresponding error

$$\epsilon_{V_{\text{rms}}} \equiv \frac{1}{V_{\text{rms}}} \sqrt{(V_{\text{los}} \epsilon_{V_{\text{los}}})^2 + (\sigma_{\text{los}} \epsilon_{\sigma_{\text{los}}})^2}.$$

We discarded the bins with values of V_{los} and σ_{los} with relative uncertainties $\epsilon_{V_{\text{los}}}/V_{\text{los}} > 1$ and $\epsilon_{\sigma_{\text{los}}}/\sigma_{\text{los}} > 1$. In both galaxies, the maximum uncertainty on V_{rms} never exceeds $\epsilon_{V_{\text{rms}}} \sim 8 \text{ km s}^{-1}$. Finally, we symmetrized the resulting values with respect to the disc major axis by means of the Python algorithm PLOTBIN. We show the V_{rms} maps of NGC 4264 and NGC 4277 in the top left-hand panels of Figs 3 and 4, respectively.

We modelled the total mass distribution of both galaxies as the sum of two components

$$\rho = \rho_* + \rho_{\text{halo}},$$

where ρ_* is the mass volume density of matter (either luminous or dark) that is distributed like the stars and ρ_{halo} is the mass volume density of DM distributed in a spherical halo. We built a set of mass-follows-light models by assuming that the mass volume density ρ_* follows the luminosity volume density ν_* derived by deprojecting the intrinsic surface brightness distribution obtained from the MGE

$$\rho_* = (M/L)_* \nu_*$$

These models have three free parameters that are optimized while matching the observed V_{rms} . They are i_{disc} , $(M/L)_*$, and β_z . We adopted radially constant values for both $(M/L)_*$ and β_z .

Then, we included the contribution of the DM halo ρ_{halo} , for which we considered

(i) a quasi-isothermal (QI; Binney & Tremaine 1987) radial profile of the mass volume density

$$\rho_{\text{QI}}(r) = \frac{\rho_0}{1 + \left(\frac{r}{r_c}\right)^2},$$

where ρ_0 and r_c are the central mass volume density and core radius, respectively.

(ii) a NFW radial profile of the mass volume density

$$\rho_{\text{NFW}}(r) = \frac{\rho_s}{\frac{r}{r_s} \left(1 + \frac{r}{r_s}\right)^2},$$

where ρ_s and r_s are the scale mass volume density and scale radius, respectively. We reduced the number of free parameters by adopting the following parametrization

$$\rho_{\text{NFW}}(r) = \frac{M_{\text{vir}}}{4\pi A(c_{\text{vir}})} \cdot \frac{1}{r(r_s + r)},$$

where the virial mass M_{vir} and coefficient $A_{c_{\text{vir}}}$ are respectively given by

$$M_{\text{vir}} = \frac{4\pi}{3} r_{\text{vir}}^3 \rho_{\text{crit}} \Omega_M \Delta_{\text{vir}},$$

with $\rho_{\text{crit}} = 1.37 \times 10^{-7} M_\odot \text{ pc}^{-3}$, $\Omega_M = 0.27$ and $\Delta_{\text{vir}} = 200$, and

$$A(c_{\text{vir}}) = \log(1 + c_{\text{vir}}) - \frac{c_{\text{vir}}}{1 + c_{\text{vir}}},$$

where $c_{\text{vir}} = r_{\text{vir}}/r_s$ is the concentration parameter. We followed the $M_{\text{vir}} - c_{\text{vir}}$ relation by Klypin, Trujillo-Gomez & Primack (2011) to derive

$$c_{\text{vir}} = 9.6 \left(\frac{0.7 M_{\text{vir}}}{10^{12}} \right)^{-0.075}.$$

In this way, the mass model has only a free parameter M_{vir} .

(iii) a generalized NFW (gNFW; Barnabè et al. 2012) radial profile of the mass volume density

$$\rho_{\text{gNFW}}(r) = \rho_s \left(\frac{r}{r_s}\right)^\gamma \cdot \left(\frac{1}{2} + \frac{1}{2} \frac{r}{r_s}\right)^{-(\gamma+3)},$$

where ρ_s and r_s are the scale mass volume density and scale radius, respectively, while the γ parameter gives the inner slope of the radial profile. We constrained it in the range $-2 < \gamma < 0$, with $\gamma = 0$ corresponding to a cored profile and $\gamma = -1$ to a NFW profile.

For each mass model, we computed the radial profiles of the enclosed mass and circular velocity for the stars, DM in the halo, and their sum. We used Monte Carlo simulations to estimate the 1σ confidence intervals. At each radius, we generated a distribution of enclosed mass and circular velocity taking into account the errors on the best-fitting parameters of the mass model. The adopted $\pm\sigma$ errors of enclosed mass and circular velocity for the stars, DM in the halo, and their sum are calculated as the 16th and 84th percentiles of the distributions.

For the three mass models with a DM halo, we calculated the fraction of DM within the bar region as

$$f_{\text{DM,bar}} = \frac{M_{\text{DM}}(r < a_{\text{bar}})}{M_{\text{DM}}(r < a_{\text{bar}}) + M_*(r < a_{\text{bar}})}.$$

We calculated the corresponding $\pm\sigma$ errors as the 16th and 84th percentiles of the distribution of $f_{\text{DM,bar}}$ that we built from the same Monte Carlo simulations previously generated.

The JAM code allows the inclusion of the contribution of a central supermassive black hole (SMBH), which is modelled through the MGE formalism as a Gaussian having mass M_\bullet , axial ratio $q = 1$ and $3\sigma \lesssim r_{\text{min}}$, with r_{min} defined as the smallest distance from the SMBH that can be chosen $r_{\text{min}} \sim \sigma_{\text{PSF}}$ (Cappellari 2008, 2020). Due to the limited spatial resolution of the available ground-based kinematic observations, we cannot constrain the mass M_\bullet of the central SMBH. Therefore, we decided to adopt the SMBH mass value given by the $M_\bullet - \sigma_e$ relation (Kormendy & Ho 2013). We estimated the bulge effective velocity dispersion from the MUSE kinematic map and the

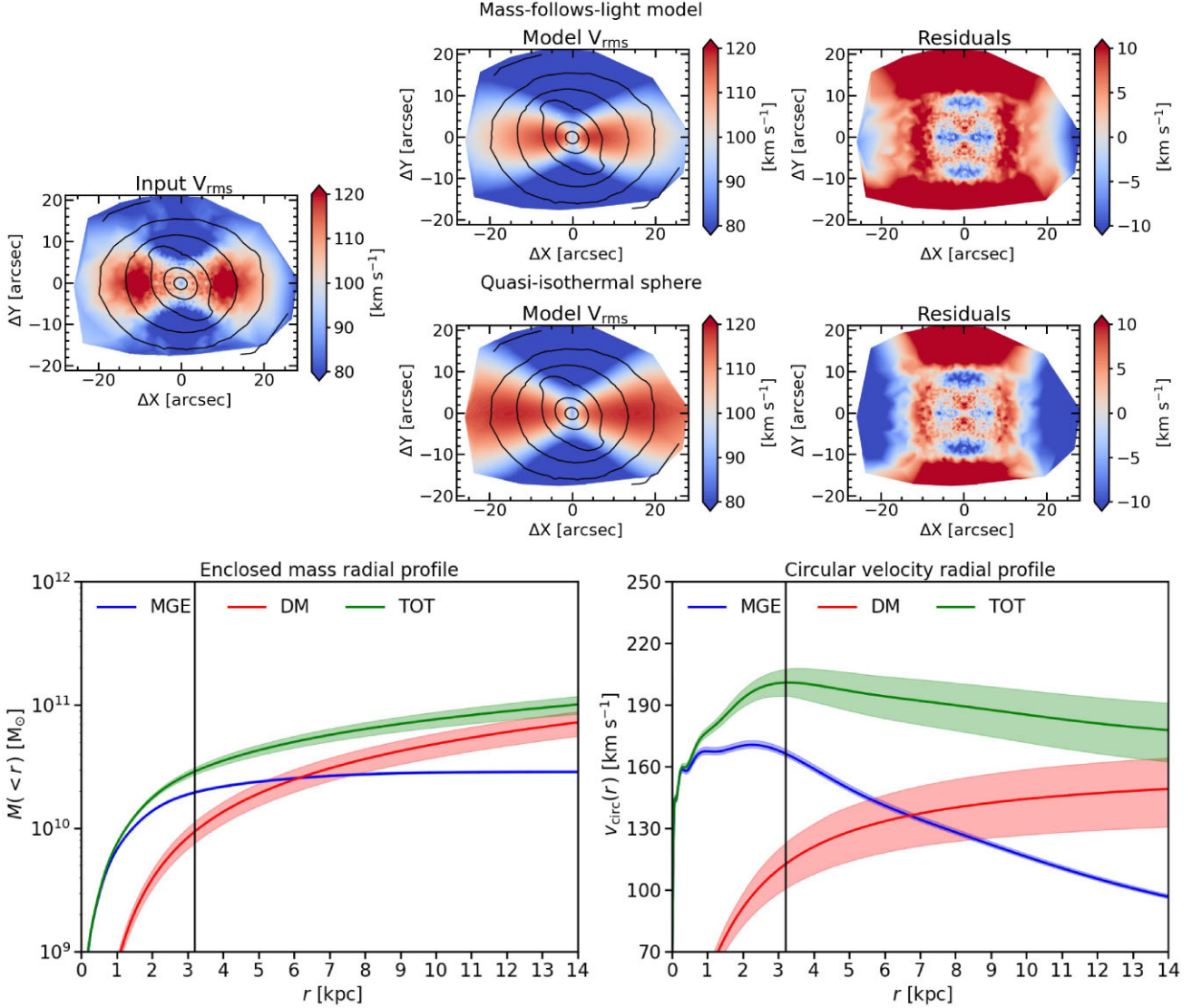


Figure 3. Top panels: Symmetrized V_{rms} from the MUSE stellar kinematics of NGC 4264 (left panel), bisymmetric second velocity moment predicted by the mass-follows-light model (top-centre panel) and by the mass model with a QI halo (bottom-centre panel), and residuals of the observed and modelled V_{rms} (top right-hand and bottom right-hand panels). Bottom panels: Radial profiles of enclosed mass (left-hand panel) and circular velocity (right-hand panel) of NGC 4264 for the mass model with a QI halo. The contributions of the stars (blue line) and DM (red line) are plotted with their sum (green line). The vertical solid and dashed lines mark the bar radius and the extension of kinematic data, respectively. The shaded areas represent the $\pm\sigma$ errors calculated from Monte Carlo simulations.

reconstructed image as the luminosity-weighted average of the observed V_{rms} inside an elliptical region with a semimajor axis equal to half of the bulge effective radius $R_{\text{e, bulge}}$ and the same axial ratio q_{bulge} of the bulge. We adopted the values obtained by Cuomo et al. (2019a) and Buttitta et al. (2022) with a parametric photometric decomposition of the SDSS images of NGC 4264 ($R_{\text{e, bulge}} = 1.53$ arcsec, $q_{\text{bulge}} = 0.77$) and NGC 4277 ($R_{\text{e, bulge}} = 1.77$ arcsec, $q_{\text{bulge}} = 0.84$).

5 RESULTS

For both galaxies, we obtained the best-fitting parameters for all the mass models without and with a DM halo. We analysed the mass-follows-light models as well as the models with a QI, NFW, and gNFW DM halo to constrain the DM fraction within the bar region of NGC 4264 and NGC 4277.

5.1 NGC 4264

We construct a starting set of mass models by considering the galaxy inclination as a free parameter. The mass models with a DM halo return the same value (QI, gNFW) or a value consistent within errors (NFW) with that obtained by Cuomo et al. (2019a) from the isophotal analysis of NGC 4264 ($i_{\text{disc}} = 36^\circ 7$), whereas the mass-follows-light model gives a much larger value ($i = 42^\circ 9 \pm 1^\circ 3$).

We repeat the analysis after masking the kinematic bins within a circular region of radius $r = 8$ arcsec, which corresponds to the bar radius projected onto the sky plane. In this way, we consider only the kinematic data measured in the disc region. But, all the mass models converge to an edge-on solution with $\beta_z \sim -1.45$ as a consequence of the inclination-anisotropy degeneracy (Krajnović et al. 2005; Lablanche et al. 2012). We verify that this result is not driven by the twisted structure of the disc of NGC 4264. The

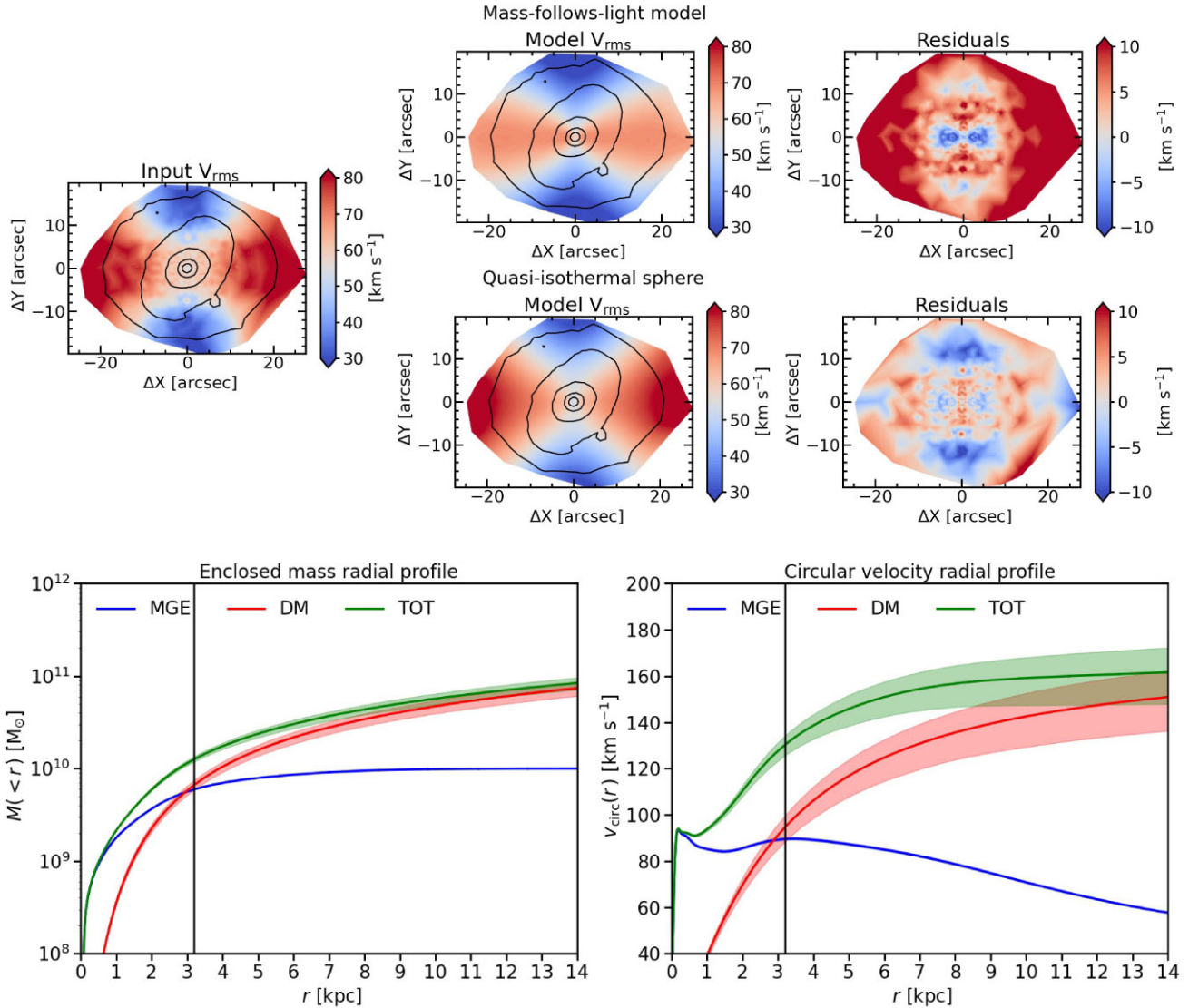


Figure 4. Same as Fig. 3, but for NGC 4277.

kinematic bins in the external disc ($r > 25$ arcsec) account for less than 1 per cent of the data and the mass models based on a different MGE decomposition of the SDSS image, where we mask the external disc, do not improve the fit. We perform a further sanity check by masking the kinematic bins in the central circular region of radius $r = 2.5$ arcsec to minimize biases due to an uncorrected estimation of the PSF and/or the SMBH mass. Then, we decide to fix the inclination to build the final set of mass models. We adopt $i = 36.5$ which corresponds to the photometric value of Cuomo et al. (2019a). An intrinsic flattening $q_0 = 0.05$ is adopted in JAM modelling to derive i from the observed axial ratio, whereas i_{disc} is obtained by Cuomo et al. (2019a) assuming an infinitesimally thin disc. The choice of a fixed inclination allows a straightforward comparison between the best-fitting parameters of the different mass models, which we list in Table 3 together with their reduced χ^2 .

We find a slightly larger mass-to-light ratio for the mass-follows-light model ($(M/L)_*$, $i \sim 2.6 M_{\odot} L_{\odot}^{-1}$) with respect to the mass models with a DM halo ($(M/L)_*$, $i \sim 2.1 M_{\odot} L_{\odot}^{-1}$). This is expected if there is a small amount of DM, which is not distributed like the stars. Since we are interested in recovering the mass distribution of NGC 4264

and not in its orbital structure, we were not concerned by the fact that the mass-follows-light model was not able to constrain β_z and the mass models with the DM halo returned a remarkably negative value of anisotropy ($\beta_z \sim -7.3$).

The observed V_{rms} is characterized by a central local minimum of $\sim 90 \text{ km s}^{-1}$ with a remarkable double-peaked structure with a maximum of $\sim 120 \text{ km s}^{-1}$ at $|r| \sim 15$ arcsec along the galaxy major axis decreasing to $\sim 80 \text{ km s}^{-1}$ at $|r| \gtrsim 20$ arcsec (Fig. 3, left-hand panel). Although the overall shape of the isovelocity contours is reproduced by the mass-follows-light model (Fig. 3, top-centre panel), it fails to match the location and amplitude of the double peak of V_{rms} (Fig. 3, top right-hand panel). The mass models with a DM halo provide a better fit to the observed V_{rms} (Fig. 3, bottom-centre panel), although they do not correctly reproduce the decrease measured at large radii along the galaxy major axis (Fig. 3, bottom right-hand panel). At face value, the mass model with the QI halo is marginally better than those with the NFW ($\Delta\chi^2_v = 0.09$) and gNFW halo ($\Delta\chi^2_v = 0.01$).

The DM fraction within the bar of the best-fitting model is $f_{\text{DM,bar}}^{\text{QI}} = 0.33 \pm 0.04$, which is compatible, within 1σ uncertainty,

Table 3. Best-fitting parameters of the mass models of NGC 4264 and NGC 4277. Bracket values refer to fixed parameters, while unconstrained values (having relative errors larger than 1) are labelled.

Model	Parameter		NGC 4264	NGC 4277
mass-follows-light	$(M/L)_{*,i}$	$(M_{\odot} L_{\odot}^{-1})$	2.55 ± 0.02	2.36 ± 0.05
	i	($^{\circ}$)	(36.5)	(40.6)
	β_z	–	unc.	unc.
	χ^2_{ν}	–	5.54	5.81
QI	$(M/L)_{*,i}$	$(M_{\odot} L_{\odot}^{-1})$	2.18 ± 0.05	1.72 ± 0.02
	$\log_{10}(\rho_0/M_{\odot} \text{pc}^{-3})$	–	-0.61 ± 0.13	-1.04 ± 0.04
	r_c	(kpc)	1.33 ± 0.28	2.46 ± 0.24
	i	($^{\circ}$)	(36.5)	(40.6)
	β_z	–	-7.12 ± 1.73	-1.48 ± 0.19
	χ^2_{ν}	–	3.98	1.54
	$f_{\text{DM, bar}}$	–	0.33 ± 0.04	0.53 ± 0.02
	NFW	$(M/L)_{*,i}$	$(M_{\odot} L_{\odot}^{-1})$	2.14 ± 0.03
$\log_{10}(M_{200}/M_{\odot})$		–	13.94 ± 0.12	13.33 ± 0.05
i		($^{\circ}$)	(36.5)	(40.6)
β_z		–	-7.86 ± 1.99	-1.55 ± 0.20
χ^2_{ν}		–	4.07	1.62
$f_{\text{DM, bar}}$		–	0.35 ± 0.01	0.56 ± 0.01
gNFW	$(M/L)_{*,i}$	$(M_{\odot} L_{\odot}^{-1})$	2.14 ± 0.05	1.69 ± 0.04
	$\log_{10}(\rho_s/M_{\odot} \text{pc}^{-3})$	–	-1.20 ± 0.15	-2.14 ± 0.36
	r_s	(kpc)	2.25 ± 0.53	11.3 ± 6.6
	γ	–	(0)	-0.34 ± 0.26
	i	($^{\circ}$)	(36.5)	(40.6)
	β_z	–	-6.86 ± 1.65	-1.49 ± 0.19
	χ^2_{ν}	–	3.99	1.55
	$f_{\text{DM, bar}}$	–	0.34 ± 0.05	0.53 ± 0.18

with that predicted by the mass models with a NFW ($f_{\text{DM, bar}}^{\text{NFW}} = 0.35 \pm 0.01$) and gNFW halo ($f_{\text{DM, bar}}^{\text{gNFW}} = 0.34 \pm 0.05$). This suggests that the mass budget of NGC 4264 is baryon-dominated in the radial range mapped by the kinematic data. We show in the top panels of Fig. 3 the maps of the second velocity moments predicted of the best-fitting mass models of NGC 4264 without and with a QI halo to be compared with the map of observed V_{rms} . The corresponding radial profile of the enclosed mass and circular velocity for the stars, DM, and their sum are given in the bottom panels of Fig. 3 for the best-fitting mass model with the QI halo.

The circular velocity profile in the region between the bar end and the edge of the kinematic data ($3 \leq r \leq 5$ kpc) is characterized by a weak decline. This means that, in this radial range, the DM halo does not play a dominant role with respect to the luminous component. This is a local trend which has been commonly observed in galaxies with massive bulges, with more luminous galaxies having on average more strongly declining rotation curves. At large radii, however, all declining rotation curves flatten out, indicating that substantial amounts of DM must be present in these galaxies too (Noordermeer et al. 2007; Kalinova et al. 2017; Frosst et al. 2022).

For the QI model, the contribution of DM starts to dominate the mass budget far beyond the bar region at a galactocentric distance $r \gtrsim 7$ kpc). As a further check of our dynamical modelling, we derive the mean circular velocity of the inner disc in the radial range ($3.3 \leq r \leq 4.2$ kpc) adopted by Cuomo et al. (2019a) to estimate the circular velocity by correcting the stellar streaming motion for asymmetric drift. We find $V_{\text{circ}}^{\text{QI}} = 200 \pm 7 \text{ km s}^{-1}$ which is consistent within 2σ error with the asymmetric drift estimate $V_{\text{circ}}^{\text{AD}} = 189 \pm 10 \text{ km s}^{-1}$ by Cuomo et al. (2019a).

We compare our results with those obtained by Cappellari et al. (2013), who modelled NGC 4264 using a JAM mass model with

a NFW halo. Their stellar kinematics maps were obtained with the SAURON integral-field spectrograph, covering a smaller FOV ($0.55 \times 0.7 \text{ arcmin}^2$) and having a lower angular resolution (FWHM = 1.5 arcsec) with respect to ours. Nevertheless, Cappellari et al. (2013) reported that the DM fraction within the galaxy’s effective radius ($R_e = 13.4 \text{ arcsec}$) is $f_{\text{DM}}(r < R_e) = 0.31$ with a maximum circular velocity of $V_{\text{circ, max}} = 191 \text{ km s}^{-1}$. We find a consistent value of $f_{\text{DM}}^{\text{NFW}}(r < R_e) = 0.28 \pm 0.01$, but a larger value of $V_{\text{circ, max}}^{\text{NFW}} = 260 \pm 4 \text{ km s}^{-1}$ for the mass model with a NFW halo. The discrepancy between the two values of the circular velocity could due to the different extensions of the adopted data.

5.2 NGC 4277

As done for NGC 4264, we construct a starting set of mass models by considering the galaxy inclination as a free parameter. Considering the intrinsic flattening, the mass models with a DM halo return a consistent value ($i = 40^{\circ}.6$) with that obtained by Buttiitta et al. (2022) from the isophotal analysis of NGC 4277 ($i_{\text{disc}} = 40^{\circ}.7$), whereas the mass-follows-light model gave $i = 46^{\circ}.3 \pm 6^{\circ}.0$. We verify that all the mass models recovered the photometric inclination after masking the kinematic bins belonging to the bar-dominated region ($r < 8 \text{ arcsec}$). In this way, we rely only on the kinematic bins of the disc. We perform a further check by masking the central kinematic bins ($r < 2.5 \text{ arcsec}$) to avoid issues related to the wrong PSF and/or the SMBH mass and we find the same model parameters. Finally, we decide to fix the inclination to build the final set of mass models. We adopt the value consistent with the photometric estimate to allow a straightforward comparison between the best-fitting parameters of the different mass models, which are given in Table 3 together with the reduced χ^2 of the mass models.

We find a much larger mass-to-light ratio for the mass-follows-light model ($(M/L)_{*,i} \sim 2.4 M_{\odot} L_{\odot}^{-1}$) with respect to the mass models with a DM halo ($(M/L)_{*,i} \sim 1.7 M_{\odot} L_{\odot}^{-1}$). This is expected if there is DM in addition to the stars. We are not able to constrain β_z with the mass-follows-light model, whereas all the mass models with a DM halo returned the same negative value within errors for the anisotropy ($\beta_z \sim -1.5$).

Although more than 60 per cent of the kinematic bins of NGC 4277 are located in the bar-dominated region, where the stars are expected to dominate the galaxy mass (Fig. 4, left-hand panel), the predicted second velocity moment of the mass-follows-light model does not match the observed V_{rms} in terms of amplitude ($V_{\text{rms}} \sim 80 \text{ km s}^{-1}$ for $r \gtrsim 12$ arcsec) and shape of the isoveLOCITY contours (Fig. 4, top-centre panel), contrary to the models with a DM halo (Fig. 4, bottom-centre panel). Therefore, we conclude that the best-fitting mass model of NGC 4277 requires a DM halo. As for NGC 4264, the mass model with the QI halo fits slightly better than those with the NFW ($\Delta\chi^2 = 0.08$) and gNFW halo ($\Delta\chi^2 = 0.01$). The DM fraction within the bar is $f_{\text{DM,bar}}^{\text{QI}} = 0.53 \pm 0.02$ which is fully consistent with the fractions predicted by the mass models with a NFW ($f_{\text{DM,bar}}^{\text{NFW}} = 0.56 \pm 0.01$) and gNFW DM halo ($f_{\text{DM,bar}}^{\text{gNFW}} = 0.53 \pm 0.18$). These findings suggest that NGC 4277 hosts a considerable amount of DM, which is not tied to the stars, within the radial range mapped by the kinematic data. This holds no matter the adopted radial profile of the DM mass volume density. We argue that the large amount of DM in the inner regions of NGC 4277 is responsible for the slowdown of its bar.

We show in the top panels of Fig. 4 the maps of the second velocity moments predicted by the best-fitting mass models of NGC 4277 without and with the QI halo to be compared with the map of observed V_{rms} . The corresponding radial profile of the enclosed mass and circular velocity for the stars, DM, and their sum of the best-fitting mass model with the QI halo are shown in the bottom panels of Fig. 4.

The contribution of the DM starts to dominate the mass budget just outside the bar region ($r \gtrsim 3$ kpc) and the circular velocity flattens out at a larger galactocentric distance ($r \gtrsim 5$ kpc) as expected for a DM-dominated region. We derive the mean value $V_{\text{circ}}^{\text{QI}} = 136 \pm 4 \text{ km s}^{-1}$ of the circular velocity in the same radial range ($2.1 \leq r \leq 5.9$ kpc) adopted by Butti et al. (2022) to estimate the circular velocity by correcting the stellar streaming motion for asymmetric drift. They found $V_{\text{circ}}^{\text{AD}} = 148 \pm 5 \text{ km s}^{-1}$. The two values are consistent with each other within 2σ errors.

6 CONCLUSIONS

We have built Jeans axisymmetric dynamical models for the two barred lenticular galaxies NGC 4264 and NGC 4277. They are very similar in terms of morphology, size, and luminosity. But NGC 4264 hosts a fast bar, which nearly extends out to its corotation ($\mathcal{R} = 0.9 \pm 0.2$; Cuomo et al. 2019a), while the bar embedded in NGC 4277 is slow and falls short of the corotation ($\mathcal{R} = 1.8^{+0.5}_{-0.3}$; Butti et al. 2022). We focused on these galaxies because their bar pattern speeds are amongst the best-constrained ones obtained with direct measurements through the Tremaine-Weinberg method (Tremaine & Weinberg 1984). We considered both mass-follows-light models and mass models with a spherical halo of DM, which is not tied to the stars, by matching the stellar kinematics obtained with the MUSE integral-field spectrograph and using SDSS images to recover the stellar mass distribution.

For both galaxies, the best-fitting mass model has a quasi-isothermal halo for which we derived the fraction of dark matter

$f_{\text{DM,bar}}$ within the bar region. This is the first time that \mathcal{R} is measured along with $f_{\text{DM,bar}}$ obtained from dynamical modelling. We found that the inner regions of NGC 4277 host a larger amount of dark matter ($f_{\text{DM,bar}} \sim 0.5$) with respect to NGC 4264 ($f_{\text{DM,bar}} \sim 0.3$) in agreement with the predictions of theoretical works and the findings of numerical simulations. Indeed, fast bars are expected to live in baryon-dominated discs, whereas slow bars have experienced a strong drag from the dynamical friction due to a dense halo of dark matter. First, Weinberg (1985) predicted that a DM halo with a significant central mass density exerts a dynamical torque on the bar causing its slowdown. Similar results were later confirmed by several works based on N-body simulations (Debattista & Sellwood 1998, 2000; Athanassoula & Misiriotis 2002; Martinez-Valpuesta et al. 2017; Petersen et al. 2019). The bar in a less massive DM halo could require a longer time-scale to be slowed down. Tailoring numerical simulations to well-studied galaxies like NGC 4264 and NGC 4277 will make it possible to track the decrease of the bar pattern speed as a function of the DM content and to predict the present value of \mathcal{R} to be compared with observations.

According to the results of numerical simulations, tidally induced bars are typically slower than those spontaneously formed by internal instabilities (Miwa & Noguchi 1998; Martinez-Valpuesta et al. 2017; Łokas 2018). Martinez-Valpuesta et al. (2017) found that bars formed after coplanar flybys with massive companions typically have a rotation rate $\mathcal{R} > 1.8$. Similarly, large rotation rates characterize the bars formed in the numerical experiments of Łokas (2018), which explored the case of retrograde encounters of two galaxies with comparable mass. Butti et al. (2022) argued that the formation of the slow bar in NGC 4277 could be induced by the close companion NGC 4273. NGC 4277 does not present strong evidence of tidal interaction with the nearby galaxy, therefore it is not possible to confirm this scenario. However, we can conclude that the large DM fraction in its inner regions influenced the evolution of the bar driving it to an even slower regime. On the other hand, Cuomo et al. (2019a) pointed out that the mild interaction with NGC 4261 favours the spontaneous formation of the fast bar of NGC 4264. We conclude that the low DM fraction in the bar-dominated region was not enough to efficiently slow down the bar to the slow regime.

Following theoretical results (e.g. Athanassoula et al. 2013; Sellwood 2014) angular momentum is exchanged at resonances, but it is emitted at the inner resonances and absorbed at the outer ones. However, the estimate of the amount of angular momentum exchanged at the resonances would require tracking the temporal evolution of the bar parameters of NGC 4264 and NGC 4277 through tailored N-body simulations. Nevertheless, it is possible to estimate the amount of DM enclosed within the corotation radius. The location of the corotation and bar radius of NGC 4264 are consistent with each other within errors, whereas the corotation radius of NGC 4277 is about twice as large as the bar radius. For NGC 4264, the DM fraction enclosed within the corotation radius ($f_{\text{DM,cor}} = 0.29 \pm 0.04$) is the same within errors as that enclosed within the bar radius ($f_{\text{DM,bar}} = 0.33 \pm 0.04$). On the contrary, for NGC 4277 the DM fraction enclosed within the corotation radius ($f_{\text{DM,cor}} = 0.72 \pm 0.03$) is much larger than that inside the bar radius ($f_{\text{DM,bar}} = 0.53 \pm 0.02$) further supporting our conclusions.

A systematic application of the JAM algorithm to simulated barred galaxies with bars of different orientations, lengths, strengths, and pattern speeds is required to extend the parameter space explored by Lablanche et al. (2012). This is needed to understand the uncertainties and biases on the dynamical parameters, including the DM content in the bar-dominated region, for a given galaxy configuration. In

particular, the regimes of weakly barred galaxies and dwarf-barred galaxies, which give a major contribution to the galaxy population, are yet to be explored.

This is a crucial step to extend this dynamical analysis to all the barred galaxies with a measured bar rotation rate from integral-field spectroscopic data, like those targeted by CALIFA (Sánchez et al. 2012; Aguerri et al. 2015; Cuomo et al. 2019b), MANGA (Bundy et al. 2015; Guo et al. 2019; Garma-Oehmichen et al. 2020, 2022), and PHANGS-MUSE (Williams et al. 2021; Emsellem et al. 2022). With a large set of modelled galaxies, it will be possible to look for a quantitative relationship between \mathcal{R} and $f_{\text{DM, bar}}$ with the aim of using \mathcal{R} as a diagnostic of the DM content in galaxy discs.

Finally, NGC 4264 and NGC 4277 are amongst the barred galaxies with the best-studied bar properties in terms of surface-brightness distribution, stellar kinematics, and mass modelling. For this reason, they are ideal candidates to be adopted as a test bench in applying the orbit-superposition Schwarzschild dynamical models, which have been recently developed for tumbling bars by Vasiliev & Valluri (2020) and Tahmasebzadeh et al. (2022) but which have been applied to date only to mock galaxies created from N-body simulations.

ACKNOWLEDGEMENTS

We thank the referee for a very constructive report that helped us to improve the manuscript. CB, EMC, and AP are supported by Italian Ministry for Education University and Research (MIUR) grant Progetto di Ricerca di Interesse Nazionale (PRIN) 2017 20173ML3WW-001 and Padua University grants Dotazione Ordinaria Ricerca (DOR) 2019-2021. JALA and LC are supported by the Spanish Ministerio de Ciencia e Innovación y Universidades by the grants PID2020-119342GB-I00 and PGC2018-093499-B-I00, respectively. LC acknowledges financial support from Comunidad de Madrid under Atracción de Talento grant 2018-T2/TIC-11612. VC is supported by Fondecyt Postdoctoral programme 3220206–2022 and by ESO-Chile Joint Committee programme ORP060/19. The analysis in this paper was realized with the use of the Python packages ASTROPY (Astropy Collaboration 2018), MATPLOTLIB (Hunter 2007), NUMPY (McKinney 2010), and SCIPY (van der Walt, Colbert & Varoquaux 2011). The MGE decomposition and JAM dynamical models were performed with the Python packages MGEFIT (Cappellari 2002) and JAMPY (Cappellari 2008). Funding for the Sloan Digital Sky Survey IV has been provided by the Alfred P. Sloan Foundation, the US Department of Energy Office of Science, and the Participating Institutions. SDSS-IV acknowledges support and resources from the Center for High-Performance Computing at the University of Utah. The SDSS web site is www.sdss.org. SDSS-IV is managed by the Astrophysical Research Consortium for the Participating Institutions of the SDSS Collaboration including the Brazilian Participation Group, the Carnegie Institution for Science, Carnegie Mellon University, the Chilean Participation Group, the French Participation Group, Harvard-Smithsonian Center for Astrophysics, Instituto de Astrofísica de Canarias, The Johns Hopkins University, Kavli Institute for the Physics and Mathematics of the Universe (IPMU)/University of Tokyo, Lawrence Berkeley National Laboratory, Leibniz Institut für Astrophysik Potsdam (AIP), Max-Planck-Institut für Astronomie (MPIA Heidelberg), Max-Planck-Institut für Astrophysik (MPA Garching), Max-Planck-Institut für Extraterrestrische Physik (MPE), National Astronomical Observatories of China, New Mexico State University, New York University, University of Notre-Dame, Observatório Nacional/MCTI, The Ohio State University, Pennsylvania State University, Shanghai Astronomical Observatory, United Kingdom Participation Group, Universidad

Nacional Autónoma de México, University of Arizona, University of Colorado Boulder, University of Oxford, University of Portsmouth, University of Utah, University of Virginia, University of Washington, University of Wisconsin, Vanderbilt University, and Yale University.

DATA AVAILABILITY

The derived data in this article will be shared on request to CB.

REFERENCES

- Abolfathi B. et al., 2018, *ApJS*, 235, 42
Aguerri J. A. L. et al., 2000, *A&A*, 361, 841
Aguerri J. A. L., Debattista V. P., Corsini E. M., 2003, *MNRAS*, 338, 465
Aguerri J. A. L., Méndez-Abreu J., Corsini E. M., 2009, *A&A*, 495, 491
Aguerri J. A. L. et al., 2015, *A&A*, 576, A102
Algorry D. G. et al., 2017, *MNRAS*, 469, 1054
Astropy Collaboration, 2018, *AJ*, 156, 123
Athanassoula E., 1992, *MNRAS*, 259, 345
Athanassoula E., Misiriotis A., 2002, *MNRAS*, 330, 35
Athanassoula E., Machado R. E. G., Rodionov S. A., 2013, *MNRAS*, 429, 1949
Barnabè M. et al., 2012, *MNRAS*, 423, 1073
Binney J., Tremaine S., 1987, *Galactic Dynamics*. Princeton Univ. Press, Princeton
Bundy K. et al., 2015, *ApJ*, 798, 7
Buta R. J. et al., 2015, *ApJS*, 217, 32
Buttitta C. et al., 2022, *A&A*, 664, L10
Cappellari M., 2002, *MNRAS*, 333, 400
Cappellari M., 2008, *MNRAS*, 390, 71
Cappellari M., 2020, *MNRAS*, 494, 4819
Cappellari M., Copin Y., 2003, *MNRAS*, 342, 345
Cappellari M., Emsellem E., 2004, *PASP*, 116, 138
Cappellari M. et al., 2011, *MNRAS*, 413, 813
Cappellari M. et al., 2013, *MNRAS*, 432, 1709
Chilingarian I. V., Zolotukhin I. Y., 2012, *MNRAS*, 419, 1727
Corsini E. M., 2011, *Mem. Soc. Astron. Ital.*, 18, 23
Cuomo V. et al., 2019a, *MNRAS*, 488, 4972
Cuomo V., Lopez Aguerri J. A., Corsini E. M., Debattista V. P., Méndez-Abreu J., Pizzella A., 2019b, *A&A*, 632, A51
Cuomo V., Aguerri J. A. L., Corsini E. M., Debattista V. P., 2020, *A&A*, 641, A111
Debattista V. P., Sellwood J. A., 1998, *ApJ*, 493, L5
Debattista V. P., Sellwood J. A., 2000, *ApJ*, 543, 704
Debattista V. P., Mayer L., Carollo C. M., Moore B., Wadsley J., Quinn T., 2006, *ApJ*, 645, 209
de Lorenzi F., Debattista V. P., Gerhard O., Sambhus N., 2007, *MNRAS*, 376, 71
de Vaucouleurs G., de Vaucouleurs A., Corwin H. G., Jr, Buta R. J., Paturel G., Fouqué P., 1991, *Third Reference Catalogue of Bright Galaxies*. Springer, New York
de Zeeuw P. T. et al., 2002, *MNRAS*, 329, 513
Emsellem E. et al., 2022, *A&A*, 659, A191
Fixsen D. J., Cheng E. S., Gales J. M., Mather J. C., Shafer R. A., Wright E. L., 1996, *ApJ*, 473, 576
Fragkoudi F., Athanassoula E., Bosma A., 2016, *MNRAS*, 462, L41
Fragkoudi F., Grand R. J. J., Pakmor R., Springel V., White S. D. M., Marinacci F., Gomez F. A., Navarro J. F., 2021, *A&A*, 650, L16
Frosst M., Courteau S., Arora N., Stone C., Macciò A. V., Blank M., 2022, *MNRAS*, 514, 3510
Garma-Oehmichen L., Cano-Díaz M., Hernández-Toledo H., Aquino-Ortiz E., Valenzuela O., Aguerri J. A. L., Sánchez S. F., Merrifield M., 2020, *MNRAS*, 491, 3655
Garma-Oehmichen L. et al., 2022, *MNRAS*
Gerhard O. E., 1993, *MNRAS*, 265, 213
Gerhard O. E., Binney J. J., 1996, *MNRAS*, 279, 993

- Gottloeber S., Hoffman Y., Yepes G., 2010, Wagner S., Steinmetz M., Bode A., Muller M.M., eds, *High Performance Computing in Science and Engineering*, Springer, p. 309
- Grand R. J. J. et al., 2017, *MNRAS*, 467, 179
- Guo R., Mao S., Athanassoula E., Li H., Ge J., Long R. J., Merrifield M., Masters K., 2019, *MNRAS*, 482, 1733
- Hunter J. D., 2007, *Comput. Sci. Eng.*, 9, 90
- Kalinova V. et al., 2017, *MNRAS*, 469, 2539
- Kim S. et al., 2014, *ApJS*, 215, 22
- Klypin A. A., Trujillo-Gomez S., Primack J., 2011, *ApJ*, 740, 102
- Kormendy J., Ho L. C., 2013, *ARA&A*, 51, 511
- Krajnović D., Cappellari M., Emsellem E., McDermid R. M., de Zeeuw P. T., 2005, *MNRAS*, 357, 1113
- Lablanche P.-Y. et al., 2012, *MNRAS*, 424, 1495
- Laurikainen E., Salo H., Buta R., Knapen J. H., 2007, *MNRAS*, 381, 401
- Łokas E. L., 2018, *ApJ*, 857, 6
- Marioni O. F., Abadi M. G., Gottlöber S., Yepes G., 2022, *MNRAS*, 511, 2423
- Martinez-Valpuesta I., Aguerri J. A. L., González-García A. C., Dalla Vecchia C., Stringer M., 2017, *MNRAS*, 464, 1502
- McKinney, 2010, in van der Walt S., Millman J., eds, *Proceedings of the 9th Python in Science Conference*. SciPy, Austin, TX, p. 56
- Méndez-Abreu J. et al., 2017, *A&A*, 598, A32
- Miwa T., Noguchi M., 1998, *ApJ*, 499, 149
- Navarro J. F., Frenk C. S., White S. D. M., 1995, *MNRAS*, 275, 56
- Nelson D. et al., 2018, *MNRAS*, 475, 624
- Noguchi M., 1987, *MNRAS*, 228, 635
- Noordermeer E., van der Hulst J. M., Sancisi R., Swaters R. S., van Albada T. S., 2007, *MNRAS*, 376, 1513
- Pagotto I., Corsini E. M., Sarzi M., Pagani B., Dalla Bontà E., Morelli L., Pizzella A., 2019, *MNRAS*, 483, 57
- Petersen M. S., Weinberg M. D., Katz N., 2019, *MNRAS*, 490, 3616
- Pillepich A. et al., 2018, *MNRAS*, 475, 648
- Portail M., Gerhard O., Wegg C., Ness M., 2016, *MNRAS*, 465, 1621
- Prugniel P., Soubiran C., 2001, *A&A*, 369, 1048
- Roshan M., Ghafourian N., Kashfi T., Banik I., Haslbauer M., Cuomo V., Famaey B., Kroupa P., 2021, *MNRAS*, 508, 926
- Rybicki G. B., 1987, in de Zeeuw P. T. ed., *Proc. IAU Symp. 127, Structure and Dynamics of Elliptical Galaxies*. Springer, Dordrecht, p. 397
- Sánchez S. F. et al., 2012, *A&A*, 538, A8
- Sarzi M. et al., 2006, *MNRAS*, 366, 1151
- Schaye J. et al., 2015, *MNRAS*, 446, 521
- Schlaflly E. F., Finkbeiner D. P., 2011, *ApJ*, 737, 103
- Schmitt H. R., 2001, *AJ*, 122, 2243
- Scott N. et al., 2013, *MNRAS*, 432, 1894
- Sellwood J. A., 1981, *A&A*, 99, 362
- Sellwood J. A., 2014, *Rev. Mod. Phys.*, 86, 1
- Tahmasebzadeh B., Zhu L., Shen J., Gerhard O., van de Ven G., 2022, *ApJ*, 941, 109
- Tremaine S., Weinberg M. D., 1984, *ApJ*, 282, L5
- Vasiliev E., Valluri M., 2020, *ApJ*, 889, 39
- van Driel W., Ragaïne D., Boselli A., Donas J., Gavazzi G., 2000, *A&AS*, 144, 463
- van der Marel R. P., Franx M., 1993, *ApJ*, 407, 525
- van der Walt S., Colbert S. C., Varoquaux G., 2011, *Comput. Sci. Eng.*, 13, 22
- Weinberg M. D., 1985, *MNRAS*, 213, 451
- Williams M. J., Bureau M., Cappellari M., 2009, *MNRAS*, 400, 1665
- Williams T. G. et al., 2021, *AJ*, 161, 185
- Willmer C. N. A., 2018, *ApJS*, 236, 47

This paper has been typeset from a $\text{\TeX}/\text{\LaTeX}$ file prepared by the author.